ElectroThermal Subsurface Gas Generation and Transport: Model Validation and Implications

Water Resources Research

RESEARCH ARTICLE
10.1029/2018WR024095

Electro-Thermal Subsurface Gas Generation and Transport: Model Validation and Implications

Ian L. Molnar[1], **Kevin G. Mumford**[2], **and Magdalena M. Krol**[1]

[1]Lassonde School of Engineering, York University, Toronto, Ontario, Canada, [2]Department of Civil Engineering, Queen's University, Kingston, Ontario, Canada

Key Points:
- Coupled Macroscopic Invasion Percolation (MIP) model with continuum heat and mass models accurately reproduced lab-scale gas production and migration
- Simulation of condensation mechanisms and heat recirculation within gas clusters were key to capturing gas flow dynamics with MIP
- Higher concentrations of dissolved oxygen and nitrogen increased gas mobilization and decreased steam condensation rates in cold water

Supporting Information:
- Supporting Information S1

Correspondence to:
M. M. Krol,
magdalena.krol@lassonde.yorku.ca

Citation:
Molnar, I. L., Mumford, K. G., & Krol, M. M. (2019). Electro-thermal subsurface gas generation and transport: Model validation and implications. *Water Resources Research*, *55*, 4630–4647. https://doi.org/10.1029/2018WR024095

Received 13 SEP 2018
Accepted 27 APR 2019
Accepted article online 6 MAY 2019
Published online 7 JUN 2019

Abstract Gas generation and flow in soil is relevant to applications such as the fate of leaking geologically sequestered carbon dioxide, natural releases of methane from peat and marine sediments, and numerous electro-thermal remediation technologies for contaminated sites, such as electrical resistance heating. While traditional multiphase flow models generally perform poorly in describing unstable gas flow phenomena in soil, Macroscopic Invasion Percolation (MIP) models can reproduce key features of its behavior. When coupled with continuum heat and mass transport models, MIP has the potential to simulate complex subsurface scenarios. However, coupled MIP-continuum models have not yet been validated against experimental data and lack key mechanisms required for electro-thermal scenarios. Therefore, the purpose of this study was to (a) incorporate mechanisms required for steam generation and flow into an existing MIP-continuum model (ET-MIP), (b) validate ET-MIP against an experimental lab-scale electrical resistance heating study, and (c) investigate the sensitivity of water boiling and gas (steam) transport to key parameters. Water boiling plateaus (i.e., latent heat), heat recirculation within steam clusters, and steam collapse (i.e., condensation) mechanisms were added to ET-MIP. ET-MIP closely matched observed transient gas saturation distributions, measurements of electrical current, and temperature distributions. Heat recirculation and cluster collapse were identified as the key mechanisms required to describe gas flow dynamics using a MIP algorithm. Sensitivity analysis revealed that gas generation rates and transport distances, particularly through regions of cold water, are sensitive to the presence of dissolved gases.

1. Introduction

Gas generation and flow in the subsurface are strongly coupled to a complex suite of processes including groundwater flow, heat transport, and mass transport. The coupling of these processes governs the system-level behavior of applications such as in situ thermal treatment (ISTT) of contaminated sites (e.g., Hegele & McGee, 2017; Krol et al., 2014), methane ebullition in peat bogs (e.g., Chen & Slater, 2015), marine and freshwater sediments (e.g., Keller & Stallard, 1994; Liu et al., 2016; Mogollón et al., 2009), and leakage from geological carbon storage systems (e.g., Oldenburg & Unger, 2003; Zuo et al., 2017).

The design and application of electrical resistance heating (ERH), a popular ISTT technology (Kingston et al., 2010), require an understanding of the coupled mechanisms shown in Figure 1 to treat a contaminated site. Figure 1 illustrates the processes and material properties interlinking ERH's state variables. Figure 1 does not represent a mass or energy flowchart but instead illustrates where the interlinking arises from and which system variables they influence. For instance, ERH heats the groundwater system to water-boiling temperatures through the application of an electrical current. Gas is generated when the temperature of the system is high enough for the total vapor pressure to exceed the confining pressure (sum of capillary and water pressures). The elevated temperature co-boils volatile nonaqueous phase liquids with water and the generated steam strips dissolved volatile organic compounds (VOCs) out of the groundwater (Beyke & Fleming, 2005). As the boiling process continues, gas clusters will expand until buoyancy forces are strong enough to overcome capillary forces and mobilize the gas. Gas flow may then occur as either continuous channels or discontinuous clusters move toward extraction points. Groundwater flow may retard the heating process and prevent steam formation or collapse steam channels (Hegele & McGee, 2017); when either unheated groundwater flows into a heated zone or when gas flows upward into unheated zones, the groundwater lowers the gas' temperature and gas collapse may happen when vapor pressure drops below the confining pressure. Subsequently, groundwater flow patterns will change both during heating (i.e., buoyant groundwater flow; Krol, Sleep, Johnson, 2011), and in response

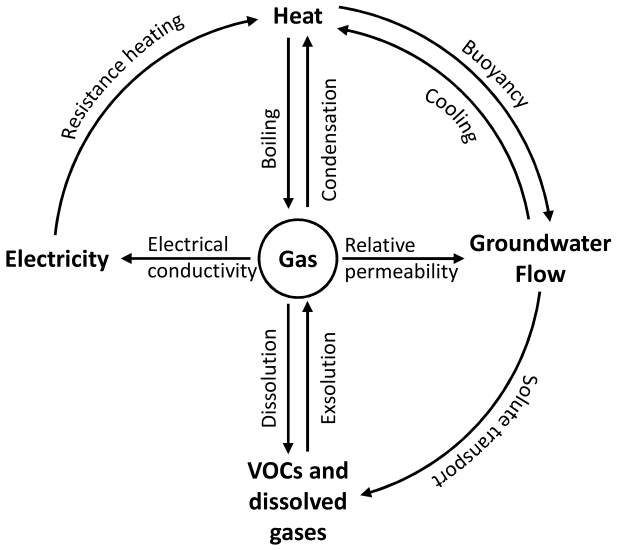

Figure 1. A conceptual model of the state variables (bolded text) and interlinking processes and material processes (text above linking arrows) that govern groundwater flow, gas generation, and volatile organic carbon (VOC) removal during electrical resistance heating (ERH).

to gas generation (i.e., lower relative permeability; Zhao & Ioannidis, 2011). This shifting groundwater flow pattern has been shown to redistribute heat and contaminant mass (Krol, Mumford, et al., 2011; Krol, Sleep, Johnson, 2011; Krol et al., 2014). Likewise, gas generation alters the electrical conductivity (Archie, 1942), changing heating patterns.

Several numerical models have been developed specifically to optimize solutions to the highly coupled problems illustrated in Figure 1. The model by McGee and Vermeulen (2007) focuses on the distribution of electrical heating rates in groundwater during ERH but does not include gas generation and groundwater flow. The Electro-Thermal Model (ETM) by Krol, Mumford, et al. (2011); Krol, Sleep, & Johnson, (2011); Krol et al. (2014) is capable of electrical heating, buoyant flow, and discrete gas generation and groundwater flow. The TOUGH2 (Pruess et al., 1999) and NUFT (Hao et al., 2012) families of models are continuum multiphase models that specialize in simulating coupled flow processes in variably saturated/unsaturated scenarios and have been used for simulating water boiling processes (Baston et al., 2010), air sparging (Geistlinger et al., 2009), steam enhanced extraction (Falta et al., 1992), and CO_2 storage (Doughty, 2007; Johnson et al., 2004). NUFT also has a specific module for ERH (Hao et al., 2012) based on the work of Carrigan and Nitao (2000). CompSim (Sleep & Sykes, 1993) is also a continuum multiphase model for simulating coupled thermal/groundwater systems and has been employed for hot water flushing (O'Carroll & Sleep, 2007).

With the exception of ETM, the above models are either single-phase (i.e., fully water saturated) or employ a multiphase continuum extension of Darcy's law. While multiphase Darcy's law can describe transient gas flow when it is governed by continuous channels or stable displacement fronts, it is generally unable to capture the detailed distribution of unstable and dynamic gas flows (e.g., channels and clusters; McCray & Falta, 1997; Thomson & Johnson, 2000; Geistlinger et al., 2009; Stauffer et al., 2009), limiting its applicability for subsurface gas applications.

Strong buoyancy forces acting on subsurface gas create a capillary pressure gradient that can destabilize upward gas movement (Geistlinger et al., 2006; Stöhr & Khalili, 2006), resulting in the formation of gas fingers and channels, or discrete bubbles capable of mobilization (Brooks et al., 1999; Clayton, 1998; Elder & Benson, 1999; Roosevelt & Corapcioglu, 1998). These bubbles typically exist as multipore gas clusters rather than bubbles that occupy a single pore body. Discontinuous gas clusters are typically formed in coarser soils (Brooks et al., 1999; Ji et al., 1993) and at slow gas flow rates (Geistlinger et al., 2006; Mumford et al., 2009; Stöhr & Khalili, 2006). This may result in highly complex behavior where a mobilized gas cluster undergoes repeated fragmentation and coalescence events (Stöhr & Khalili, 2006), temporary immobilization (i.e., capillary trapping; Stöhr & Khalili, 2006), and possible collapse due to local heat or mass transfer (Krol, Mumford, et al., 2011; Mumford et al., 2010).

Within gas channels and discrete clusters, gas exists at a relatively high saturation (Geistlinger et al., 2009; Mumford et al., 2009) with a sharp, step-like drop in gas saturation outside the cluster or channel. However, continuum multiphase flow models predict smooth variations in saturation, creating gas distributions at lower saturations that are spread over larger areas than the characteristic step-like change in gas saturation experimentally observed in channels and clusters (Geistlinger et al., 2009). As a result, continuum multiphase models are able to match experimentally observed total gas volumes, but their inadequate description of the smaller-scale gas processes means they struggle to accurately reproduce experimentally observed gas velocities and local gas saturations (Lassen et al., 2015).

The inability of continuum multiphase models to capture the discrete features of subsurface gas, including gas flow velocity and local saturations, limits their applicability for subsurface gas applications. Gas-based remediation technologies (including thermal technologies) require an accurate understanding of the gas flow distribution to design gas extraction points to account for channelized or unstable flow rather than flow as a continuous distribution (Tomlinson et al., 2003). In addition, gas flow is sensitive to subsurface

heterogeneity (e.g., Ji et al., 1993; Munholland et al., 2016) creating the potential for lateral spreading and release in unexpected and highly localized locations (Lassen et al., 2015; Munholland et al., 2016; Tomlinson et al., 2003). For example, dissolution and condensation processes impact gaseous carbon emissions to the atmosphere (e.g., methane, CO_2; Mogollón et al., 2009; Lassen, Plampin, et al., 2015; Lassen, Sonnenborg, et al., 2015; Cahill et al., 2017) and extraction of volatilized contaminants (Hegele, 2014; Krol, Mumford, et al., 2011; Mumford et al., 2010; Munholland et al., 2016; Roy & Smith, 2007). Predicting dissolution behavior requires accurate estimation of the pore-scale and macroscale distributions of the fluid phases (e.g., Agaoglu et al., 2016; Grant & Gerhard, 2007; Nambi & Powers, 2000). As a result, models unable to incorporate the discrete, unstable, and dynamic features of gas flow may not produce optimal outcomes.

Despite their limitations, modifications to continuum multiphase models have been reported to successfully reproduce gas generation and flow data under some conditions. Stauffer et al. (2009) reproduced some features of gas injection with a series of sub–representative elementary volume (REV) stochastic simulations although Samani (2012) suggests that this approach may overestimate simulated gas volumes. Amos and Mayer (2006) generated gas with the method from Cirpka and Kitanidis (2001) and successfully reproduced experimental 1-D water table fluctuation experiments; however, their model only considered groundwater flow. Enouy et al. (2011) reproduced 1-D CO_2 gas flow experiments using a combination of multiphase Darcy's law and an empirical correlation for mass transfer between gas and water phases.

Discrete models such as invasion percolation (IP) have been more successful in modeling unstable gas flow as they can be modified to explicitly incorporate buoyancy-driven gas flow, as well as gas cluster fragmentation, coalescence, mobilization, and expansion (Glass & Yarrington, 2003; Tsimpanogiannis & Yortsos, 2004; Wagner et al., 1997; Xu et al., 1998). While traditional IP models are applied at the pore-scale, other studies have demonstrated that IP can be upscaled to describe gas cluster growth and mobilization at the macroscopic scale (MIP; Kueper & McWhorter, 1992; Yortsos et al., 1993; Ewing & Berkowitz, 2001; Mumford et al., 2010; Krol, Mumford, et al., 2011; Mumford et al., 2015). Whereas IP models determine gas displacement events from the curvature of individual pore throats, water drainage and imbibition events in MIP are based on locally assigned P_c-S_w relationships and an entry pressure that has been averaged across a REV. In applications of both IP and MIP, it is assumed that viscous forces are negligible, as occurs for slow gas velocities.

Krol, Mumford, et al. (2011) demonstrated that the MIP approach could be coupled with a continuum ETM model (ET-MIP) to simulate gas formation during heating of water and dissolved VOC mixtures at sub-water boiling temperatures; this coupling was achieved by combining the ideal gas law, Henry's law, and Dalton's law to describe gas formation and then utilizing variably saturated descriptions of groundwater flow, electrical conductivity, and heat and mass transport. Their simulations reproduced experimentally observed behavior such as gas generation, fingering, VOC partitioning, and gas phase mass transport (e.g., Cirpka & Kitanidis, 2001; Clayton, 1998; Mumford et al., 2009; Mumford et al., 2010). Despite these promising results, ET-MIP requires additional modification to include mechanisms to simulate the water boiling and unstable steam transport physics that govern ISTT remediation technologies. Steam differs from the low-solubility gases typically used to study subsurface gas flow in that it requires substantial heat transfer through the gas phase to maintain its gaseous form (i.e., $T > 100$°C at 1 atm). It is common to treat liquid/steam systems in porous media as a 1-D heat pipe. Heat pipe studies have elucidated the processes driving steam behavior and heat flux in porous media, which include counter-current flow, vaporization, condensation, and gravity (e.g., Amili & Yortsos, 2004; Gomaa & Somerton, 1974; McGuinness, 1996; Satik et al., 1991; Udell, 1985). However, to the best of the authors' knowledge, these heat pipe mechanisms have not yet been incorporated into MIP models.

Since continuum models, and current MIP models, are unable to incorporate both water boiling and unstable, discrete gas flow behavior, there is a need to develop a MIP model capable of simulating water boiling and unstable steam transport. This type of model would aid optimal ISTT remediation design and improve understanding of other subsurface gas applications, including for better estimates of atmospheric emissions. In addition, few MIP models have been rigorously validated against experimental data, and no coupled MIP-continuum models have been validated. As such, the objectives of this study are to (a) extend the ET-MIP model to include mechanisms such as gas phase heat transport, cluster collapse, water boiling

plateaus, and the impact of dissolved gases on gas generation and flow; (b) validate ET-MIP against an experimental lab-scale ERH study; and (c) investigate the sensitivity of water boiling and gas (steam) transport to the presence of dissolved gases and gas saturations required for onset of gas mobilization. This extended and newly validated ET-MIP model provides one of the most complete frameworks for investigating highly coupled thermal/groundwater/mass transport and gas flow systems. The sensitivity analysis provides some of the first insights into how gas generation and coupled heat transfer mechanisms impact groundwater flow and steam channel formation.

2. Numerical Model

While some of the details of the ET-MIP model have been published elsewhere (Krol et al., 2014; Krol, Mumford, et al., 2011; Krol, Sleep, & Johnson, 2011), they will be presented here to provide a complete model of the processes governing thermal/gas/groundwater systems.

Briefly, ET-MIP is a 2-D model that couples a block-centered finite difference, implicit continuum model for energy, groundwater, and mass transport with a discrete approach for gas generation and transport. At the start of each time-step, the energy, groundwater, and gas generation equations are solved iteratively using successive over-relaxation. This iterative method is required as the solutions to the three equations are coupled (illustrated in Figure 1) with numerous temperature- and saturation-dependent parameters (e.g., density and relative permeability) that rely on the assumption that the coupled processes remain in equilibrium. Once equilibrium is achieved, any aqueous mass (e.g., dissolved gases and VOCs) is partitioned between the gas and aqueous phases using a localized equilibrium approach (i.e., Henry's law) and transported using the standard advective-dispersive formulation. The MIP routine is then called to move gas, mass, and heat throughout the domain before starting the next time step.

2.1. Energy Transport

The energy equation describes heat generation due to ERH processes, as well as heat transport within the aqueous phase. During ERH, heat is generated from power dissipated by the electrical resistivity of the subsurface. This heat generation (U) is described using (Krol, Sleep, & Johnson, 2011)

$$U = \sigma|\nabla V|^2 \tag{1}$$

where U is in J/s, σ is the electrical conductivity of the soil (S/m), and V is the electric potential. The use of U in equation (1) should not be confused with its usage in common thermodynamic notation to depict internal thermal energy. Electrical conductivity is solved using Archie's law (Archie, 1942), which describes the flow of electricity through the pore fluids of a nonconductive material. The temperature dependency of the pore water electrical conductivity is given by Arps (1953). ET-MIP's approach to describing voltage distribution is described elsewhere (Hiebert et al., 1986, 1989; Krol, Sleep, & Johnson, 2011; McGee & Vermeulen, 2007). Once the heat generation rate has been determined, the energy equation is solved for sensible heat and temperature distribution assuming local thermal equilibrium between the gas, liquid, and solid phases:

$$\frac{\partial}{\partial t}\left[S_w\rho_w\theta c_w T + (1-S_w)\rho_g\theta c_g T + (1-\theta)\rho_b c_s T - \overline{L}\right] = -c_w\rho_w\nabla\cdot\left[\overrightarrow{q}T\right] + K_H\nabla^2 T + U + Q_E \tag{2}$$

The terms ρ_w, ρ_g, and ρ_b are the densities of the water, gas, and bulk solid phases, respectively, while c_w, c_g, and c_s represents the phases' specific heat capacities; T is temperature; Q_E is a source/sink term for sensible heat; S_w is the saturation of water; $\overrightarrow{q}$ is Darcy flux vector; θ is porosity; and $\overline{L}$ represents latent heat. The left-hand side of equation (2) represents the temperature change in the soil, water, and gas phases, while the four terms on the right side represent the contributions to temperature change from convection, conduction, heat generation, and gas generation/condensation (latent heat), respectively. The description of latent heat is discussed in section 2.4. The thermal conductivity of the medium, K_H, is described by (Markle et al., 2006)

$$K_H = K_{H,s}^{(1-\theta)}K_{H,w}^{\theta} \tag{3}$$

$$K_{H,w} = 0.554 + 2.24\times10^{-3}T - 9.87\times10^{-6}T^2 \tag{4}$$

where $K_{H,s}$ and $K_{H,w}$ are the thermal conductivities of the solid and water phases, respectively. $K_{H,s}$ is expected to be a constant in the temperature ranges typical of ERH, whereas $K_{H,w}$ is temperature-dependent and given by equation (4) (Campbell et al., 1994).

2.2. Groundwater Flow

ET-MIP simulates buoyant groundwater flow by incorporating temperature-dependent water densities (ρ_w; Gebhart et al., 1988). Darcy's law is used for groundwater flow (Krol, Sleep, & Johnson, 2011):

$$\vec{q} = \frac{-kk_r g\rho_o}{\mu}\left[\nabla h_f + \frac{(\rho_w - \rho_o)}{\rho_o}\nabla \mathrm{z}\right] \tag{5}$$

where ρ_o is the reference water density at reference temperature, μ is the temperature-dependent viscosity term given by (Reid, 1977), and h_f is the equivalent freshwater head given by equation (6):

$$h_f = \frac{P}{\rho_o g} + z \tag{6}$$

The term k_r in equation (5) is the relative permeability of the water phase and is estimated using the Burdine-Brooks-Corey $k_r - S_w$ relationship (Brooks & Corey, 1966; Gerhard & Kueper, 2003).

2.3. Mass Transport

ET-MIP allows for multispecies mass transport of dissolved gases and VOCs through the aqueous phase. However, in this study only oxygen and nitrogen are considered (i.e., no VOCs). The classical advective-dispersive transport equation for a variably saturated media is employed for mass transport (Sleep & Sykes, 1993; equation (7)), with the left-hand side describing total change in mass in the water and gas phases and the right side describing transport due to advection, dispersion, and source/sink:

$$\frac{\partial}{\partial t}\left[\rho_w S_w \theta C_{w,i} + \rho_g (1 - S_w)\theta K_i C_{w,i}\right] = -\nabla\cdot\left[\rho_w C_{w,i}\vec{q}\right] + \nabla\cdot\left[\theta S_w D_{xz}\nabla C_{w,i}\right] + Q_m \tag{7}$$

where $C_{w,i}$ is the concentration of species i in the aqueous phase, K_i is a temperature-dependent gas/water partitioning coefficient for species i defined by $K_i = \frac{H_i}{RT}$ where H_i is the Henry's coefficient and R is the universal gas constant, Q_m is a mass source/sink term, and D_{xz} is the dispersion tensor for an isotropic media given by (Sleep & Sykes, 1993):

$$D_{xx,i} = \tau_d D_{d,i} + \sigma_L \frac{V_x^2}{|V|} + \sigma_T \frac{V_z^2}{|V|} \tag{8}$$

$$D_{zz,i} = \tau_d D_{d,i} + \sigma_L \frac{V_z^2}{|V|} + \sigma_T \frac{V_x^2}{|V|} \tag{9}$$

where $|V|$ is the average porewater velocity and V_x and V_z are the horizontal and vertical components of velocity, σ_L and σ_T are the longitudinal and transverse dispersivities, τ_d represents tortuosity (assumed to be uniform throughout the model domain), and $D_{d,i}$ is the molecular diffusion coefficient for aqueous species i, estimated by the ratio of viscosities (Reid, 1977):

$$\frac{D_{d,i}}{(D_{d,i})^{ref}} = \left(\frac{\mu}{\mu^{ref}}\right)^{-1.14} \tag{10}$$

where $(D_{d,i})^{\mathrm{ref}}$ and μ^{ref} are reference values for molecular diffusivity and groundwater viscosity at ambient temperature. Equation (10) modifies the molecular diffusivity ($D_{d,i}$) based on temperature via the temperature-dependent viscosity parameter (μ).

2.4. Gas-Water Partitioning and MIP Model

Gas generation and transport are solved using a discrete approach previously described by Mumford et al. (2010) and Krol, Mumford, et al. (2011). This discrete approach allows for accurate description of complex interfaces in porous media while remaining computationally efficient and relatively simple to implement.

The gas generation and transport components of ET-MIP seek to describe the governing mechanisms. Briefly, an increase in subsurface temperature increases groundwater vapor pressure; when the total vapor pressure of the system (sum of water, VOCs, and dissolved gases) exceeds the confining pressure, gas is generated. When the vapor pressure within the gas cluster is high enough to overcome the capillary pressure threshold for entry into neighboring regions, then the cluster undergoes an expansion with its volume increasing but with a corresponding decrease in pressure (via ideal gas law). However, if a cluster's gas pressure is high enough to invade a neighboring region, but capillary pressure within the cluster is low enough to allow water imbibition, then the gas cluster mobilizes; during this gas mobilization event, the total volume of the cluster does not change and any changes in pressure are a result of heat losses to the surrounding soil and groundwater. If, during expansion and mobilization, the gas cluster invades a region where the confining pressures exceed the vapor pressure (either due to high capillary pressures or cold temperatures lowering the vapor pressure), then the gas cluster collapses. If no collapse occurs, recirculation within the cluster heats the surrounding soil and groundwater in a manner similar to classical 1-D heat pipes. ET-MIP's approach to describing these mechanisms is detailed below.

2.4.1. Gas Generation

Gas is generated when the vapor pressure of the liquid exceeds the confining capillary and water pressures. ET-MIP estimates the volume of gas at each block in the model domain from a combination of Henry's law, the ideal gas law, and Dalton's law. The gas generation calculation in ET-MIP takes the form of equation (11) to solve for S_w throughout the domain for two chemical species i:

$$\sum_{i=1}^{2}\left[\frac{M_i H_i}{S_w\theta + K_i(1-S_w)\theta}\right] + P_{g,v} - P_D\left(\frac{S_w - S_r}{1-S_r}\right)^{\frac{-1}{\lambda}} - P_w = 0 \tag{11}$$

where S_r is the residual water saturation, $P_{g,v}$ is the temperature-dependent water vapour pressure determined via the Antoine equation, P_D is the displacement pressure, M_i is the total mass of a chemical species in each block, P_w is the water pressure, and λ is the pore size distribution index. Equation (11) enables gas to arise naturally from the governing physics and can thus take into account differing atmospheric pressures, subsurface heterogeneities, and the presence/absence of dissolved gases and VOCs.

The derivation of this equation is presented in the section S1 in the supporting information. However, the use of equilibrium partitioning in equation (11) results in an S_w that is independent of time step size and heating rate. In realistic boiling behavior, the volume of gas generated (or lost) is dependent upon time-step size and heating rate (i.e., faster heating results in faster gas generation). Therefore, to describe realistic boiling behavior, equation (11) must be coupled with the energy equation (equation (2)). In ET-MIP, equations (2) and (11) are coupled via latent heat. Latent heat of vaporization is the energy absorbed during water-gas phase change and the energy released during gas-water phase change. Linking equation (2) and (11) via latent heat of vaporization enables the model to capture the temperature plateau, which occurs during water boiling (100°C under standard pressure conditions; Bergman et al., 2011). The block's latent heat for two chemical species i is estimated from (Bergman et al., 2011)

$$\overline{L} = \left[\sum_{i=1}^{2}\left[L_{g,i}\rho_{g,i}\right] + L_{g,v}\rho_{g,v}\right](1-S_w)\theta \tag{12}$$

where $\overline{L}$ is the latent heat energy (J), $L_{g,i}$ is the specific latent heat for chemical species i, $L_{g,v}$ is the specific latent heat for water vapour, and $\rho_{g,i}$ and $\rho_{g,v}$ are the gas phase densities of the chemical species and water vapor estimated from the ideal gas law.

2.4.2. Gas Flow

The modified MIP algorithm presented here includes two processes specific to steam transport (Figure 2): (a) heat equilibration across a cluster and (b) steam collapse during transport into grid blocks with confining pressures greater than vapor pressures (i.e., cold blocks). These two processes transport energy from the heated zone to maintain gaseous steam fingers and provide an estimate of when steam would lose heat to the surrounding environment and collapse back to liquid water. In addition, this formulation of MIP also includes multispecies transport as well as sensible and latent heat transport. While a brief overview of this modified algorithm is provided below, a complete description of the MIP algorithm is presented in section S2.

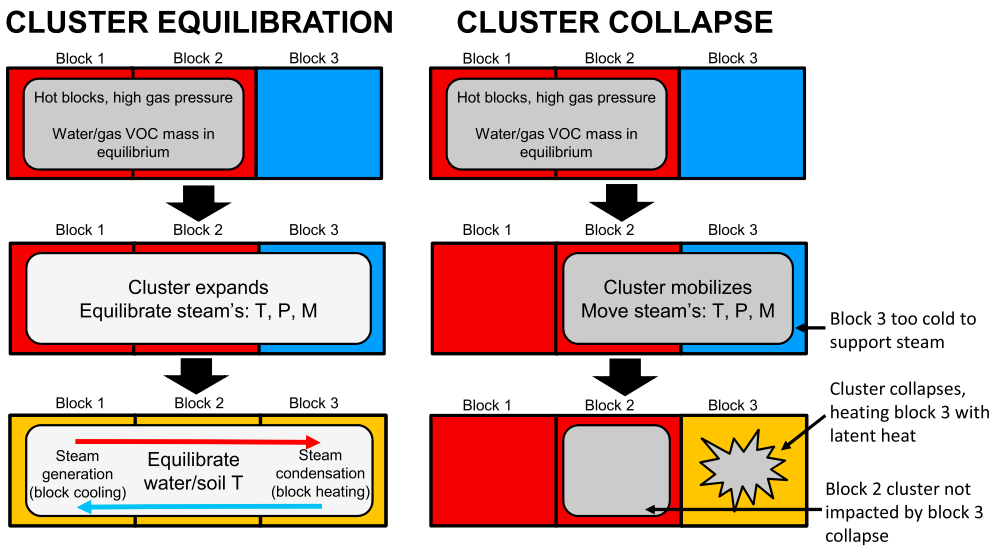

Figure 2. Illustration of the processes that occur after both expansion and mobilization events. Hot, pressurized steam clusters can either expand or mobilize based on their vapor pressures and the surrounding entry pressures. Next, the cluster's gaseous temperature (T), pressure (P), and mass (M) equilibrate. If the confining pressure of the newly invaded block is greater than the cluster's vapor pressure, that block's gas collapses (i.e., condenses). If no collapse occurs, rapid steam recirculation within the expanded or mobilized cluster causes the temperature of the soil and water across the entire cluster to reach equilibrium.

Gas saturations increase in response to higher temperatures and dissolved gas concentrations, described by equation (11). Once gas within a grid block exceeds a critical gas saturation ($S_{g,\mathrm{crit}}$), it is assumed that the gas within that block forms a connected pathway to any of the surrounding four face-sharing blocks that also have gas saturations in excess of $S_{g,\mathrm{crit}}$. During each time step, all blocks exceeding $S_{g,\mathrm{crit}}$ are tagged and adjacent tagged blocks are lumped into a single, multiblock gas cluster.

Following cluster identification, gas clusters are allowed to expand, mobilize, or fragment utilizing classic multiphase flow drainage and imbibition relationships via a set of rules described in depth by Krol, Mumford, et al. (2011), Li and Yortsos (1995), and Glass et al. (2001). Gas clusters expand when their pressure is high enough to drain the water out of an adjacent block. Mobilization occurs when the condition for expansion is met and when the water pressure is high enough to reimbibe into an area occupied by the gas cluster. This drainage and imbibition behavior is incorporated by assigning each block an initial displacement pressure (P_D), which is scaled to a temperature-dependent air/water interfacial tension (γ) (estimated from steam tables; Bergman et al., 2011). This P_D value is used to estimate the entry pressures (P_e), which is the pressure required for a gas cluster to invade a block at a gas saturation of $S_{g,\mathrm{crit}}$. It is assumed that $S_{g,\mathrm{crit}}$ is independent of a block's P_D value and is uniform across the model domain. The terminal pressure (P_T) required for water to imbibe into a block is estimated as 52% of P_e from Hegele (2014). Imbibition is assumed to return a previously gas-occupied block to 100% water saturation. The gas cluster's mass, pressure, sensible heat, and latent heat are equilibrated across the entire cluster (i.e., each block is assigned an averaged value), and the saturation within each block is adjusted to $S_{g,\mathrm{crit}}$.

Expansion of a cluster to adjacent blocks occurs when the cluster's average gas pressure exceeds the entry pressure for an adjacent block. Mobilization of a cluster occurs when the terminal pressure of a block within the cluster is greater than the entry pressure for any grid block adjacent to the cluster. This mobilization routine can also fragment clusters if the imbibed block breaks the connection between other cluster blocks. For both expansion and mobilization, the gas saturation within the newly invaded block is raised to $S_{g,\mathrm{crit}}$ and its pressure is adjusted. During mobilization, the gas saturation of the imbibed block is set to zero.

Figure 2 illustrates the processes that occur following both expansion and mobilization events. After an expansion or mobilization event, the steam's temperature, pressure, and mass (including any gaseous VOCs or dissolved gases) are equilibrated across the cluster. Gas phase advection, diffusion, convection, and conduction are not explicitly considered within ET-MIP, but rather it is assumed that heat and mass

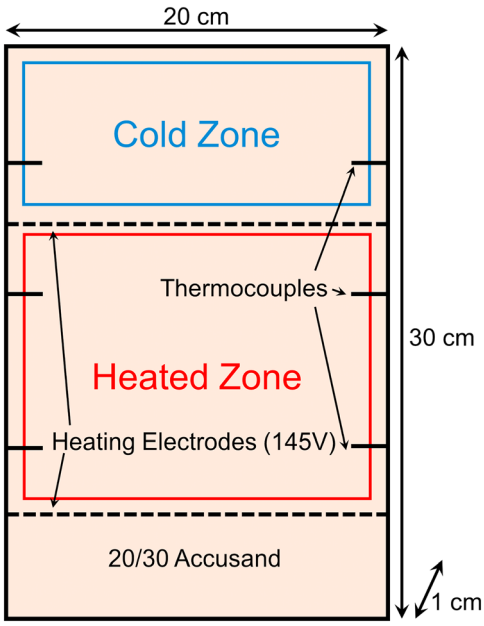

Figure 3. Configuration of the electrical resistance heating (ERH) water boiling experiment simulated by ET-MIP (*Hegele*, 2014; Hegele & Mumford, 2014). Two electrodes (dotted lines) span the water-saturated LTV cell packed with sand. The electrodes heat the sand/water region labeled 'heated zone'. Gas generated in the heated zone travels upward to the unheated region labeled 'cold zone'. Thermocouples (horizontal, solid lines) emplaced throughout the LTV cell continuously record temperatures.

distributions are in equilibrium throughout a gaseous cluster. Then, it is assumed that rapid recirculation of steam within the cluster equilibrates the temperature of the porous material and groundwater across the cluster. This equilibration process approximates the heat transfer mechanisms identified in heat pipe studies (e.g., Gomaa & Somerton, 1974; Udell, 1985). Following equilibration, every block within the cluster undergoes a collapse check; if the confining pressure of a block is greater than the total gas pressure (i.e., equation (11)), then the gas in that block collapses. For collapsed blocks, the gas saturation is set to zero and any gaseous mass within that block is added to the aqueous phase. This expansion/mobilization/equilibration/collapse process is repeated until gas clusters are no longer able to expand or mobilize. This is assumed to occur instantaneously between the transport time steps used in the continuum heat and mass transport equations. During this MIP algorithm, grid blocks may experience repeated gas cluster mobilization and collapse events in a single time-step. Each collapse event will add additional total heat (sum of sensible and latent) to the block where collapse occurs, preheating the block until it is able to maintain a steam cluster at later time. Likewise, the latent heat recirculation mechanism (Figure 2) serves to quickly transport heat from the heated zone to colder zones to help maintain open steam channels.

3. Model Validation Procedure

3.1. ERH Boiling Experiment

The ET-MIP model described in section 2 was validated against a suite of lab-scale ERH water boiling experiments presented in Hegele (2014) and Hegele and Mumford (2014). While the details of the experiments have been previously reported, they are briefly reviewed here for convenience. The experiment was conducted in a thin, water-saturated 2-D light transmission visualization cell (30×20×1cm^3; Figure 3) packed with 20/30 Accusand (d_{50} = 0.71 mm). Two graphite electrodes spanned the cell horizontally and were operated in single phase at 145V creating a 'heated zone' in the middle of the cell. Gas was generated in this heated zone and was forced to travel upwards through a 'cold zone' to reach the top of the cell where it could escape to the atmosphere. The top of the cell was covered with a perforated Teflon block that was open to the atmosphere but provided a confining pressure on the sand. The side and bottom walls of the cell were also Teflon to be electrically insulating, and the front and back of the cell were bounded by 1-cm-thick borosilicate glass walls. Thermocouples placed through the edge of the cell continuously recorded temperature in six different locations, and light transmission visualization (LTV) provided quantitative measures of gas saturation distribution throughout the cell during the experiment. A thermocouple placed outside of the LTV cell continuously recorded ambient temperatures to estimate experimental heat losses. No water flow was externally applied to the cell.

3.2. ET-MIP Implementation

Time step size was selected to meet a Courant-Friedrichs-Lewy condition, which ensure that the volume of gas generated (i.e., converted to steam) during a single time step never exceeds the pore volume of a given block. Time step size was initially set to 10 s, reduced to 1s once the maximum temperature in the domain reached 95°C, and further reduced to 0.5 s once temperatures exceeded 99°C. The spatial domain (illustrated in Figure 3) was divided into 4-×4-×10-mm grid blocks. While IP-style models are fractal in nature, a previous MIP study has indicated that a resolution of 4 mm is sufficient to produce reasonable estimates of both local gas saturations and spatial moments with a MIP model (Mumford et al., 2015). Grid independence of the continuum portion of the model (i.e., the 'ET' model) was confirmed by comparing temperature distributions of model simulations with gas production disabled across a range of resolutions. Temperature distributions changed by only ~1-2% for grid resolutions ranging 2–10 mm, indicating that grid convergence had been achieved. All boundaries of the model were assumed to be electrically insulating. The groundwater

Table 1
Initial Conditions and Model Parameters Employed by ET-MIP

Parameter	Description	Value
L_x,L_y,L_z	Domain width, height and depth (cm)[a]	20, 30, 1
dx,dy,dz	Grid discretization (cm)	0.4, 0.4, 1
dt	Time step (s)	10, 1, 0.5
T	Initial temperature[a] (°C)	26.7
l_{air}	Thickness of air buffer for heat loss[b] (cm)	0.9
τ_{elec}	Electrical tortuosity of electrode and soil blocks[b]	3.50, 1.05
θ	Porosity[a]	0.367
λ	Pore size distribution[a]	5.45
k	Permeability[3] (m^2)	2.04×10^{-10}
S_r	Irreducible water saturation[a]	0.046
ρ_b	Density of silica[d] (g/cm^3)	2.60
c_s	Specific heat of silica[d] (J/kg/K)	745
c_g	Specific heat of steam[d] (J/kg/K)	1.86×10^3
c_w	Specific heat of water[d] (J/kg/K)	4.19×10^3
$K_{H,s}$	Thermal conductivity of silica[e] (W/m/K)	8.80
σ_w^{25}	Electrical conductivity of water at 25°C[1] (μS/cm)	7540
ρ_{wall}	Density of glass and Teflon[d] (g/cm^3)	2.23, 2.20
c_{wall}	Specific heat of glass and Teflon[c,f] (J/kg/K)	835, 1200
K_{wall}	Thermal conductivity of glass and Teflon[c] (W/m/K)	1.45, 0.35
K_{air}	Thermal conductivity of air[g] (W/m/K)	0.026
L_i	Latent heat of evaporation for water, oxygen and nitrogen[4] (kJ/kg)	2,257, 213,200
σ_L,σ_T	Longitudinal and Transverse dispersivity (m)	0.002, 0.0003
$(D_d^i)^{ref}$	Molecular diffusion coefficient for O_2 and N_2[8] (m^2/s)	2.3×10^{-9}, 2.0×10^{-9}
μ^{ref}	Fluid viscosity[4] (cP)	0.89
$S_{g,crit}$	Critical gas saturation[1]	0.23
$[O_2]$	Initial oxygen concentration (mg/L)	0.88
$[N_2]$	Initial nitrogen concentration (mg/L)	1.5

[a]Hegele and Mumford (2014). [b]Fitted parameter. [c]The permeability data presented in Schroth et al. (1996) were scaled to the P_c-S_w data presented in Hegele (2014). [d]Bergman et al. (2011). [e]Markle et al. (2006). [f]DuPont Teflon PTFE (n.d.). [g]Krol, Sleep, and Johnson (2011). [h]Verhallen et al. (1984).

flow equation employed no flow boundaries for the left, right, and bottom boundaries, while the top was maintained at a constant head. Similarly, for mass transport, the left, right, and bottom boundaries were no flux and the top boundary was constant concentration (equal to initial concentrations, see Table 1) implemented with the source/sink approach described by Sleep and Sykes (1993).

For energy transport, the left, right, and bottom boundaries were modeled as no flow boundary conditions, while the top boundary was a known temperature boundary condition, set to match the ambient temperature measurements recorded throughout the experiment. However, experiments at elevated temperatures conducted in this type of thin cell are subject to heat losses through the cell walls. Experimental heat losses were estimated out the front, back, and sides of the experiment cell using a simple 1-D, explicit heat transport model modified from Krol, Sleep, & Johnson (2011); equations (13) and (14)):

$$(\rho c)_{wall}\frac{dT_{wall}}{dt} = -K_{H,\beta}\frac{d^2T}{dx} \tag{13}$$

$$U_{loss} = \frac{(\rho c)_{wall}(\Delta T_{wall})l_{wall}}{dxdt} + \frac{K_{H,air}(T_{wall}-T_{amb})}{l_{air}l_{wall}} \tag{14}$$

where U_{loss} is the total heat lost to the walls and air, $(\rho c)_{wall}$ is the density and heat capacity of the glass or Teflon walls, T_{wall} is the temperature of the glass or Teflon walls, β represents the air, soil or wall, l_{wall} is the thickness of the wall, l_{air} is the thickness of the air layer, and T_{amb} is the ambient air temperature.

The ET-MIP model presented in this study contains three fitting parameters: (a) thickness of the air layer for heat loss (l_{air}), (b) electrical tortuosity (τ_{elec}) of the blocks that contained both sand and the graphite electrodes, and (c) tortuosity of the blocks that contained just sand. These parameters were fitted to the first 30 min of experimental data, during which no gas was generated. l_{air} was fitted by comparing ET-MIP and experimental thermocouple data in the heated zone, electrical tortuosity of the bulk sand was fitted to experimental electrical current data, and tortuosity of the electrode-containing blocks was fitted to experimental thermocouple data in the cold zone. These parameters were fitted independently by minimizing the root-mean-square error. Otherwise, all model parameters were estimated either directly from experimental information or from standard literature values. Table 1 presents an overview of ET-MIP's initial conditions and model parameters.

MIP algorithms have a strong dependence on displacement pressure (P_D) distribution as gas cluster expansion and mobilization follow the paths of lowest P_D. To account for the influence of P_D behaviors on MIP predictions, the Hegele and Mumford (2014) experiments were validated against three different distributions of P_D to validate the ET-MIP model (termed 'Realization 1', 'Realization 2', and 'Realization 3'). Realizations were generated based on a cumulative distribution function from the Brooks-Corey P_c-S relationship. Figure S1 in the supporting information presents the three different P_D distributions. An initial reference displacement pressure of 10.1 cm was estimated from the P_c-S_w data presented by Hegele (2014), and a random distribution of displacement pressures was implemented based on the measured P_c-S_w curves (Glass et al., 2001; Krol, Mumford, et al., 2011; Mumford et al., 2010). The P_D values were decreased by 33% in blocks that contained the heating electrodes to account for the larger pore spaces that likely existed in those regions and resulted in observations of gas accumulation around the electrodes. The P_D values were increased by 33% in the top row of blocks to account for the smaller pore spaces that likely existed there due to local packing effects and resulted in observations of gas accumulation before exiting the sand pack (Hegele & Mumford, 2014). From these displacement pressure distributions, the permeability distributions were estimated via Leverett scaling of a

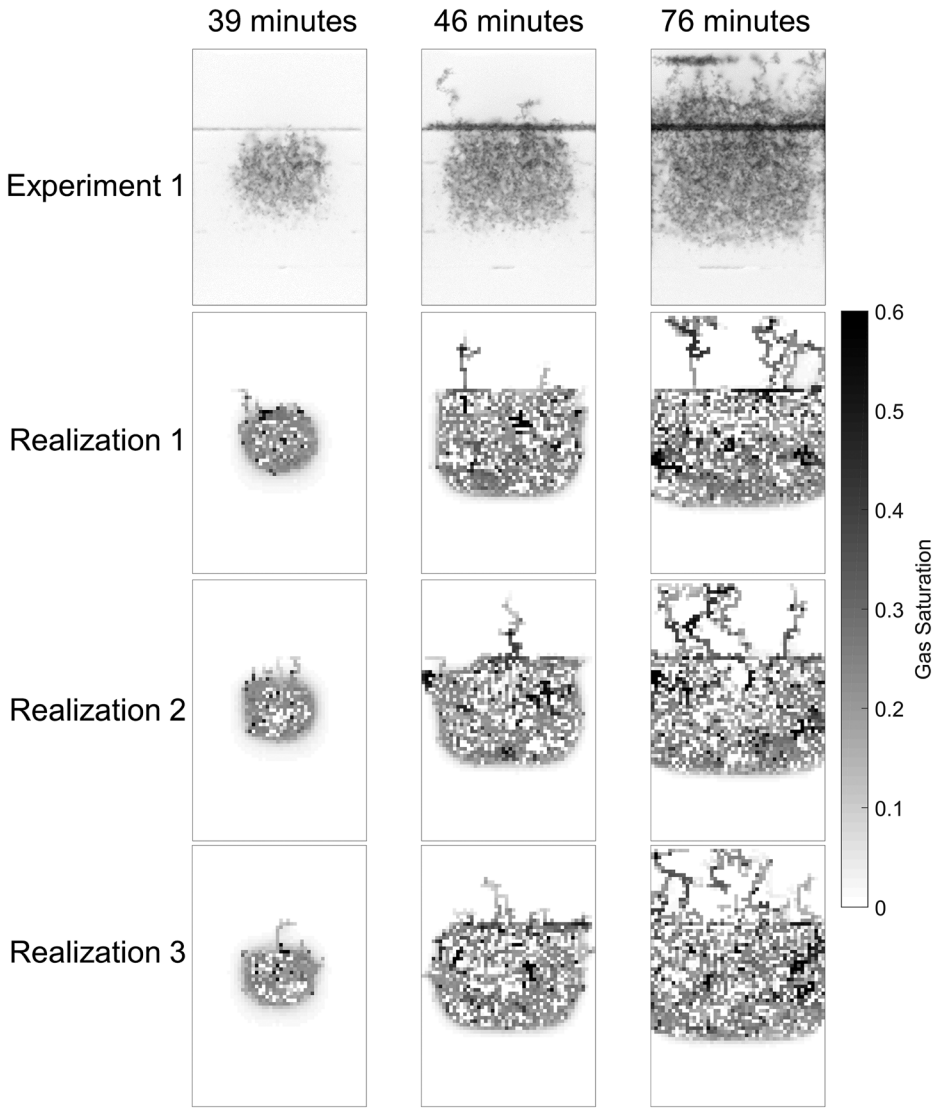

Figure 4. Gas saturation distributions from a Hegele and Mumford (2014) electrical resistance heating (ERH) experiment (top row) and the ET-MIP simulations for three different P_D distributions at three representative times.

reference permeability as described by Krol, Mumford, et al. (2011). The $S_{g,crit}$ value (see Table 1) was derived from the averaged, steady state experimental gas saturations in the heated zone. As a result, this study assumes that the experimental and simulated domains can be described with a single, homogeneous $S_{g,crit}$ value, independent of heterogeneous P_D distributions.

4. Validation of ET-MIP

4.1. Gas Saturation Distribution

Gas saturation distributions for one of the Hegele and Mumford (2014) ERH experiments and the Realizations 1, 2, and 3 ET-MIP simulations are provided in Figure 4 for three select times. Overall, the simulated gas saturation distributions show qualitative agreement with the experimental results.

Water boiling is first observed in the experiment in a small circular region in the center of the heated zone between the two electrodes (Figure 4, top row; 39 min). This water boiling region eventually expands to encompass a large portion of the heated zone (Figure 4, top row; 76 min). Heat losses at the edges delay boiling on the periphery of the heated zone. All three ET-MIP simulations exhibit the water boiling and gas generation behavior observed in the experiment. The simulated water boiling region appears at approximately

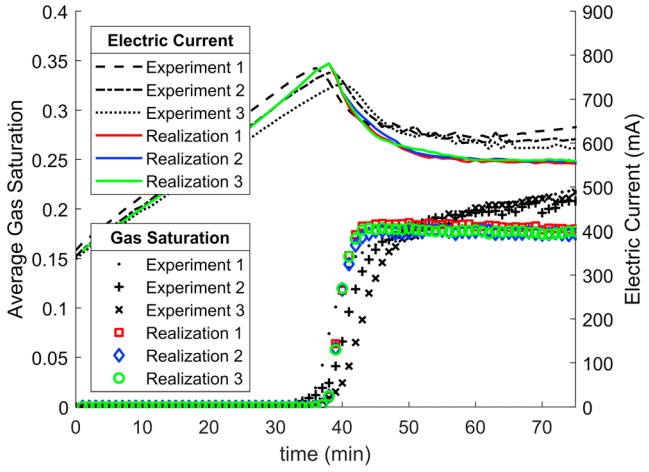

Figure 5. Electrical current and average gas saturation in the 'heated zone' indicated in Figure 3 for the ET-MIP simulations (Realizations 1, 2, and 3) and experimental data. Each ET-MIP datapoint represents multiple simulation datapoints averaged over a 1-min interval. The error bars are smaller than lines and markers and are not shown.

the same time and in the same location as the experimental water boiling region (Figure 4, 39 min) and grows at the same rate as the experiment to also encompass the majority of the heated zone (Figure 4; 46 to 76 min). This agreement between experimental and simulated gas saturation distributions within the heated zone suggests that the coupled mechanisms governing water boiling and gas generation (Figure 1) are well captured by ET-MIP and that ET-MIP can recreate the discrete variations in spatial gas saturation distributions produced by ERH during water boiling.

Buoyant gas flow features such as steam fingering, continuous channels and discrete clusters were observed throughout the experiments' cold zones (Figure 4, top row; 46 and 76 min). Hegele and Mumford (2014) noted that as the gas generated in the heated zone expanded upward, it would fragment and mobilize, creating discontinuous gas clusters. These discontinuous clusters became trapped (i.e., immobilized). Other steam fingers remained connected to the generated gas in the heated zone. These connected fingers formed continuous gas channels that eventually spanned from the heated zone to the top of the cell. At later times, a macroscopic steam front moved upward from the heated zone (Figure 4, top row; 76 min) and eventually reached the top of the cell (not shown).

The ET-MIP simulations exhibit many of the same buoyant flow features observed in the experiments (Figure 4). Once gas saturations within the heated zone reached $S_{g,crit}$, the generated gas began expanding and mobilizing upwards into the cold zone. Steam fingers and discontinuous clusters can be observed throughout the simulated cold zones, although the steam front above the top electrode was not reproduced in the simulations. The number of simulated steam fingers in Figure 4 and their growth rate is consistent with the steam fingers observed in the experiment, even though their location varies between realizations, suggesting that ET-MIP is accurately capturing both the discrete nature of buoyant flow and the dynamics. In addition, the gas saturation values within the simulated steam fingers also generally match the observed experimental steam fingers, although the consistent saturations between simulated and experimental steam fingers are likely due to ET-MIP employing the $S_{g,crit}$ derived from the experiments (Figure S2 in the supporting information illustrates that higher $S_{g,crit}$ values yield higher saturations in cold zone gas clusters).

4.2. Electrical Current and Gas Production

Electrical current, gas saturation, and temperature are strongly coupled (Figure 1; Carrigan & Nitao, 2000; Hegele & Mumford, 2014). As temperatures increase, so does the electrical current and the saturation of produced gas. However, gas production lowers temperatures (i.e., latent heat) and lowers the electrical current. Previous studies have explored this relationship through both simulations (Carrigan & Nitao, 2000) and experiments (Hegele & Mumford, 2014) and have suggested that coupled current and temperature readings are useful indicators for subsurface gas production. Figure 5 illustrates that ET-MIP accurately reproduces the experimental heated zone gas saturation and electrical current readings. In addition, all ET-MIP simulations closely match the rate of increase in the electric current as well as the peak current values. This coincides with a close match for the onset of gas production (~35 min). There is a small discrepancy in late time gas saturations (average S_g at 75 min for ET-MIP: 0.177+/- 0.0025, experiments: 0.214 +/- 0.0030) as the experimental gas saturation continues to slowly increase over time, while the simulated average gas saturations reach a steady state value after approximately 40 min. Similarly, a small discrepancy exists between simulated and experimental current values after the onset of gas production (average current [mA] at 75 min for ET-MIP: 556 +/- 3, experiments: 617 +/- 24). Both of these discrepancies are attributed to the difficulty in describing heat loss from the cell.

4.3. Temperature

Figure 6 illustrates how the simulated temperatures recreate the major features of the experimental thermocouple data. In the upper heated zone, experimental and simulated temperatures gradually increased until reaching the boiling plateau at 100°C. During this preheating phase, there is a deviation between simulated and experimental heated zone temperatures starting at approximately 25 min and reaches a maximum

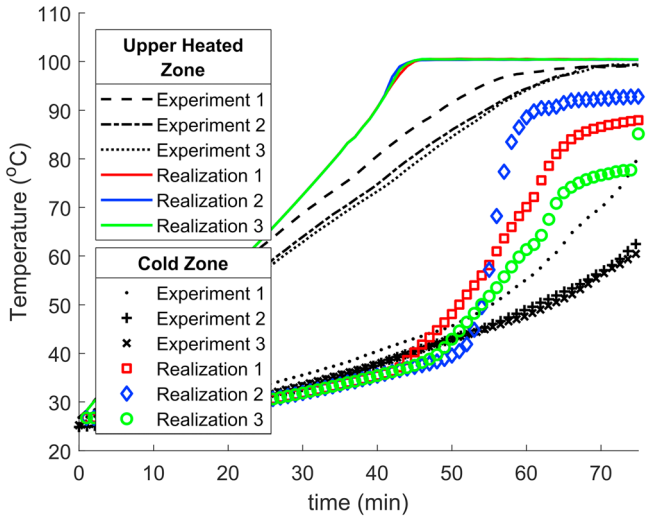

Figure 6. Thermocouple temperatures for the cold zone and upper heated zone for ET-MIP simulations and experimental results. The presented temperature data are the average temperature of the two thermocouples at each height. Each ET-MIP datapoint represents multiple simulation datapoints averaged over a 1-min interval. The error bars are smaller than lines and markers and are not shown.

difference of 15°C. While the specific cause of this deviation is unclear, it is hypothesized to be due to the simplifying assumptions required to estimate heat losses from the cell (equations (13) and (14)). Simulated temperatures reach water boiling plateaus at 100°C, consistent across all three realizations. The simulated boiling plateaus occur earlier than the experiments (simulations: 45 min, experiments: 60 min), but the presence of the temperature plateau in both simulations and experiments indicates that the latent heat mechanisms in ET-MIP are accurately capturing the water boiling physics.

Experimental cold zone thermocouples exhibit a gradual increase in temperature over time (Figure 6) as conduction and convection (from induced buoyant flow) slowly transfer heat into the cold zone. For experiments 2 and 3, this curve continues for the entire range considered in this study (76 min), although cold zone temperatures in experiment 1 increase more rapidly starting at approximately 50 min. The simulated cold zone thermocouple temperatures closely match the experimentally observed increase in temperature for the first 40 min (Figure 6). After 40-50 min the simulations undergo a rapid increase in cold zone thermocouple temperature. This rapid increase in simulated temperature is similar to the behavior in experiment 1. In the simulations, this rapid increase in temperature arises from nearby steam clusters heating the thermocouple regions. Visual inspection of the gas saturation distribution for experiment 1 suggests that a similar mechanism (i.e., heating from a nearby steam finger) is causing the rapid increase in thermocouple temperature. Figure 4 shows that large volumes of steam exist near the right cold zone thermocouple; this thermocouple increased in temperature much faster than the left thermocouple (Hegele, 2014). Visual inspections of experiments 2 and 3 in Hegele (2014) appears to confirm this behavior as they possess less steam near their cold zone thermocouples than in experiment 1 at all times and, in contrast, exhibit much slower rates of cold zone thermocouple heating. While this suggests that steam clusters are capable of rapidly transferring heat upward from the heated zone, and ET-MIP is capable of describing the major features associated with that heat transfer along steam finger, further research is required as ET-MIP appears to overestimate the rate of heating near steam fingers. This overestimation likely arises from the MIP routine's heat equilibration process approximating the heat flux mechanisms observed in heat pipes (*Udell*, 1985). While this approximation is likely accurate for small steam clusters, it may not be accurate for larger clusters. Future research on MIP steam flow would benefit from a more detailed incorporation of heat pipe transfer mechanisms.

4.4. Impact of Cluster Equilibration and Collapse Mechanics

A well-known limitation of MIP algorithms is their lack of time dependence (*Oldenburg* et al., 2016); clusters may expand and mobilize at unrealistically high velocities. Similar to these other algorithms, ET-MIP does not explicitly incorporate time dependence into its MIP algorithm. Instead, the time is constrained by the energy input that controls gas generation. Using this coupled approach, ET-MIP matched the experimentally observed gas finger distributions (Figure 4). To the best of the authors' knowledge, ET-MIP is one of the first MIP algorithms capable of matching experimentally observed gas dynamics. Other MIP formulations either did not validate to experimental data (Ganesh et al., 2013; Ioannidis et al., 1996; Koch & Nowak, 2015; Krol, Mumford, et al., 2011; Kueper & McWhorter, 1992; Mumford et al., 2010; Yortsos et al., 1993) or only demonstrated an ability to mimic static distributions of gas saturations (i.e., did not validate a single simulation against multiple experimental time steps; Ewing & Berkowitz, 2001; Mumford et al., 2015). As a result, ET-MIP is unique in its ability to capture both the discrete features of buoyant gas flow (i.e., discrete fingers and discontinuous clusters) that continuum multiphase models are unable to describe, as well as the growth rate of those features that other MIP formulations are unable to describe.

ET-MIP's ability to match experimental finger distributions at specific time intervals arises from the two mechanisms outlined in Figure 2: cluster equilibration and cluster collapse. The impact of these mechanisms on the simulated steam and heat distribution for Realization 1 is shown in Figure 7. The temperatures

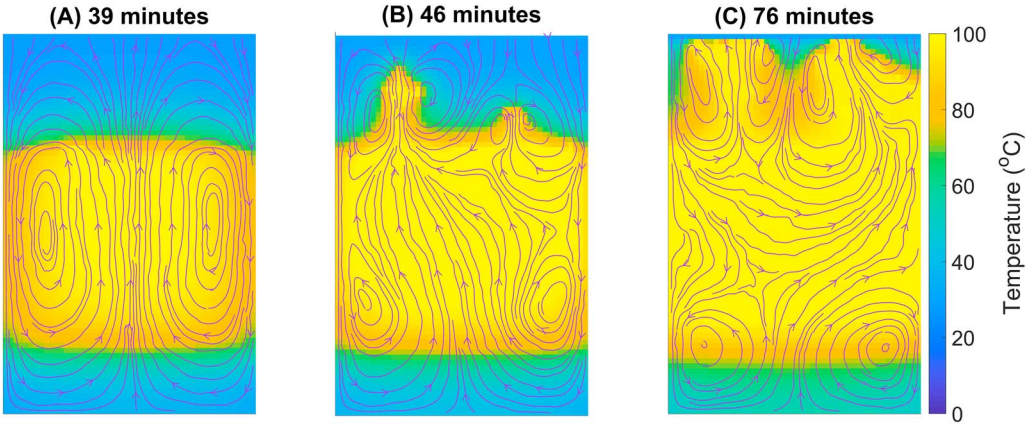

Figure 7. Temperature distributions and overlain water flow streamlines from the ET-MIP Realization 1 simulation after (a) 39 min, (b) 46 min, and (c) 76 min. The presented temperature and streamline distributions correspond to the Realization 1 gas saturation fields presented in Figure 4.

outside of the steam fingers (where heat recirculation occurs) are much lower, even in regions directly adjacent to the heated zone, demonstrating that convection and conduction in the aqueous phase alone are incapable of transferring enough heat to sustain a steam finger or cluster. In addition, preliminary simulations suggested that without a cluster equilibration term, the MIP formulation was incapable of transferring enough heat to sustain a steam finger in the cold zone for more than one time step, contrary to experimental observations. This suggests that applying MIP to thermally generated gases requires a mechanism for preheating the surrounding soil and groundwater. In addition, these preliminary simulations also suggested that without a collapse mechanism steam fingers would be capable of travelling unrealistically far distances in a single time step, also contrary to experimental observations.

While this work suggests that heat transport along steam fingers is required to match experimentally observed behavior, heat transfer along steam fingers as well as their growth into cold regions is typically neglected, as it is assumed that steam fingers rapidly lose heat and collapse (Baker, 1973; Hoffman & Kovscek, 2005; Kaluarachchi, 2000; Miller, 1975). The existence of steam fingers in cold subsurface regions have since been proven by studies on steam-assisted gravity drainage (Butler, 1987; Ito & Ipek, 2005) and ERH (Hegele & Mumford, 2014; Hegele & Mumford, 2015; Munholland et al., 2016). However, the evidence on heat transfer mechanisms within steam fingers and their relative importance versus conduction from the steam chamber/heating regions remains conflicted. Early steam-assisted gravity drainage research suggested that fingers may reach up to 6m in length and dominate heat transport into cold regions (Butler, 1987). More recent work has indicated that steam fingers are much smaller and that conduction remains the dominant heat transport mechanism (Gotawala & Gates, 2008). In the simulations presented in this study, conduction alone does not transport enough heat to match the experimentally observed steam distributions. This suggests that at the spatial and temporal scales examined in this study, heat transfer along steam fingers dominates over heat conduction from the heated zone. While the temperature distributions presented in Figure 7 suggests that heat recirculation within the gas cluster can deliver enough heat to sustain a steam cluster, the exact mechanism remains unknown and requires further study.

Previous research has explored how ERH can induce buoyant flow within the heated zone and redistribute contaminants (Krol et al., 2014; Krol, Mumford, et al., 2011; Krol, Sleep, & Johnson, 2011). However, this previous work only considered aqueous-phase convection and conductive heat transport. The streamlines overlain on the temperature distributions in Figure 7 demonstrate how groundwater flow is impacted not just by ERH within the heated zone (Figure 7a) but also by heat transfer within the steam fingers and clusters. The streamlines shift to follow finger growth, upwards flow is channeled through the zones heated by steam fingers, and downward flow occurs through the lower temperature regions outside the region impacted by steam. The experiments and simulations presented here have no externally imposed flow field; these streamlines occur only as a result of heating-induced buoyant flow, but it is expected that similar behavior would occur in realistic groundwater flow scenarios. The temperature distributions and corresponding streamlines for the other simulations are presented in the supplementary information (Figures S4-S7).

Table 2
Overview of Conducted Simulations

Simulation name	$S_{g,crit}$	$[O_2]$, initial (mg/L)	$[N_2]$, initial (mg/L)	P_D realization
Low $S_{g,crit}$-Low DG-1[a]	0.23	0.88	1.5	1
Low $S_{g,crit}$-Low DG-2[a]	0.23	0.88	1.5	2
Low $S_{g,crit}$-Low DG-3[a]	0.23	0.88	1.5	3
High $S_{g,crit}$-Low DG-1	0.30	0.88	1.5	1
Low $S_{g,crit}$-High DG-1	0.23	8.8	15	1

[a]These simulations were used for validation and were referred to as 'Realizations 1', '2', and '3' throughout section 4.

5. Sensitivity Analysis

A sensitivity analysis was performed on two parameters that are hypothesized to play key roles in governing subsurface gas flow: $S_{g,crit}$ and the concentration of dissolved gases. Sensitivity of the model results was investigated by simulating the experimental data for two $S_{g,crit}$ values (0.23 and 0.3) and two different dissolved gas concentrations (10% and 100% of equilibrium with the atmosphere at STP conditions). Table 2 provides an overview of the five simulations considered in the sensitivity analysis. Note that the simulations presented in section 4 ('Realizations 1', '2', and '3') are also included here and are renamed 'Low $S_{g,crit}$-Low DG-1', 'Low $S_{g,crit}$-Low DG-2', and 'Low $S_{g,crit}$-Low DG-3', respectively.

Gas saturation and temperature distributions for sensitivity analysis simulations High $S_{g,crit}$-Low DG-1 and Low $S_{g,crit}$-High DG-1 can be found in Figures S2, S3, S6, and S7. Figure 8 illustrates the sensitivity of the coupled gas, temperature, and electrical current relationship (illustrated in Figure 1) to both parameters. While an increased $S_{g,crit}$ value did not change the rate of heating or the peak electrical current measurements (Figure 8), it did lower the electrical current at late times by 14% relative to the low $S_{g,crit}$ simulations. This lower electrical current is due to an average gas saturation that is 28% higher than the low $S_{g,crit}$ simulations, as higher $S_{g,crit}$ values require higher gas saturations for the onset of gas flow. The increase in gas saturation is approximately equivalent to the increase in $S_{g,crit}$ between the simulations (30%). Despite the impact $S_{g,crit}$ had on heated zone gas saturations and electrical currents, $S_{g,crit}$ had no impact on thermocouple temperatures (Figure S8) and little impact on cold zone gas distribution (see Figure S2 for High $S_{g,crit}$ gas saturation distribution) relative to the Low $S_{g,crit}$-Low DG -1 simulation.

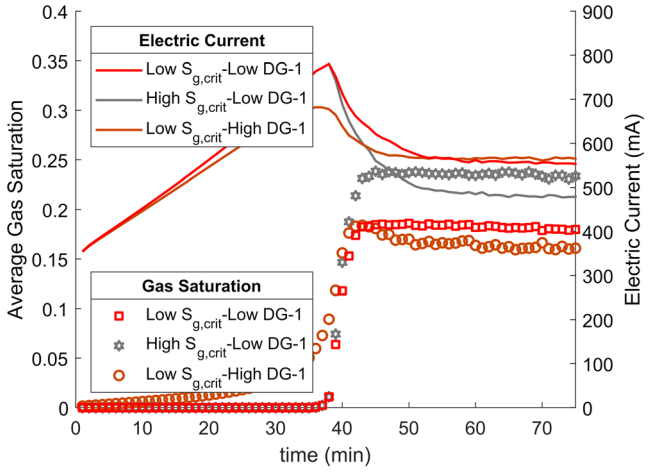

Figure 8. Electrical current and average gas saturation in the 'hot zone' indicated in Figure 3 for ET-MIP simulations and experimental data. Each ET-MIP datapoint represents multiple simulation datapoints averaged over a 1-min interval. The error bars are smaller than lines and markers and are not shown.

Increasing the concentration of dissolved gases decreased the rate of heating by a small fraction, indicated by the decreased rate of electrical current increase (Figure 8, Low DG vs High DG) during the preheating phase (0-35 min). This is likely due to the earlier and more gradual onset of gas production observed (Figure 8) as the additional dissolved oxygen and nitrogen exerted higher vapor pressures, which required lower temperatures to produce small amounts of gas. Generally, the average gas saturation in the heated zone and the electrical current trend during the gas production phase was consistent with the Low $S_{g,crit}$-Low DG -1 simulation at lower dissolved gas concentrations.

Increasing the concentration of dissolved gases had a clear impact on the gas volume within the cold zone. Figure 9 presents the gas volume in connected clusters (i.e., gas volume in grid blocks where $S_g > S_{g,crit}$). The High DG simulation had more connected gas cluster volume than any of the other simulations. At 75 min, Low $S_{g,crit}$-High DG-1 had 2.1 times more gas volume in connected clusters than the Low DG simulations. However, $S_{g,crit}$ did not significantly impact the cold zone gas volumes as the High $S_{g,crit}$-Low DG-1 simulation had similar cold zone gas volumes to the Low $S_{g,crit}$-Low DG simulations. The increase in connected cluster volume is attributed to the extra vapor pressure from the higher concentrations of oxygen and nitrogen, which helped prop open steam clusters and prevent their collapse.

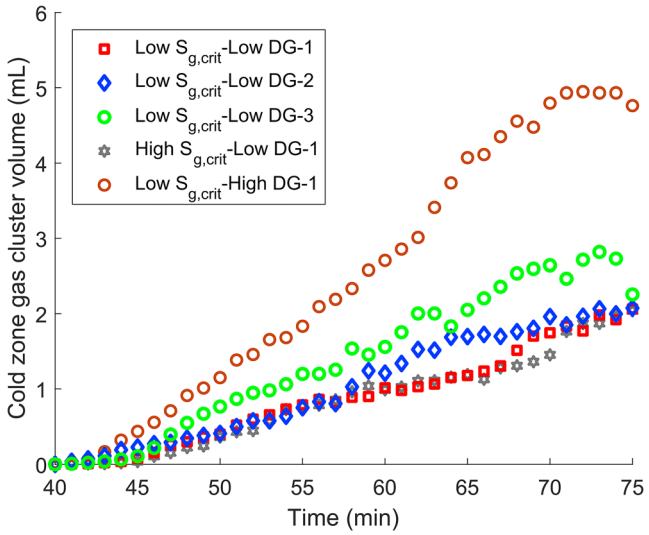

Figure 9. Gas volume in connected gas clusters (i.e., total gas volume in blocks where $S_g > S_{g,crit}$) in the cold zone indicated in Figure 3 for all ET-MIP simulations. Each datapoint represents multiple simulation datapoints averaged over a 1-min interval. The error bars are smaller than lines and markers and are not shown.

There is specific interest in understanding how dissolved gases may impact ISTT applications (such as ERH). It has been observed that rapid heat loss from steam clusters to the surrounding groundwater and soil environment may cause steam-VOC gases to collapse before they can reach extraction points, recontaminating groundwater resources and redistributing the VOCs to unexpected locations (Baker & Hiester, 2009; Hegele & Mumford, 2014; Krol, Mumford, et al., 2011; Munholland et al., 2016). It has been previously hypothesized that the addition of dissolved gases, either through exsolution or air-sparging, may decrease the risk of steam condensation and collapse (Hegele & Mumford, 2015). The results presented in Figure 9 clearly demonstrate that increasing the total vapor pressure of the system through the addition of dissolved gases facilitates the existence of steam clusters in cold regions.

6. Conclusions

This study extended a previously published model (ET-MIP), which coupled discrete gas flow to continuum temperature, groundwater, and electrical current equations, to include the mechanisms of steam production and subsequent gas flow. This model was then validated against previously published lab-scale experimental data and was subsequently used to explore the sensitivity of water boiling and steam flow behaviors to key subsurface parameters. ET-MIP reproduced the experimental gas saturation distributions in the heated zone as well as unstable gas finger distributions throughout the cold zone at various time intervals. In addition, quantitative comparisons revealed that ET-MIP closely matched temperature distributions in the experimental domain as well as quantitatively measured gas saturations and electrical current measurements. This represents one of the first thorough validations of the MIP algorithm as well as the first validation of a coupled MIP-continuum model against experimental data. IP-style models are limited to slow gas velocities. While experimental velocities of the steam fingers were not measured, the agreement between experimental and ET-MIP gas behavior indicates that the movement of in situ generated steam falls within the capillary-dominated flow regime.

Key mechanisms that enabled ET-MIP to capture these behaviors were identified to be heat recirculation within steam clusters, which provided enough heat to maintain steam channels, and steam collapse (i.e., condensation), which limited the rate at which steam fingers and clusters could grow and mobilize. Equilibration and collapse mechanisms transferred heat from the heated zone to the cold zone, which strongly impacted streamlines arising from heating-induced buoyant flow. However, comparisons of simulated and experimental thermocouple data suggest that the approach used for cluster equilibration may overestimate the rate of heat transfer within steam clusters. The lack of experimental data on steam fingering limits the ability to develop a more physically rigorous approach to heat equilibration in MIP algorithms, similar to those developed for continuum-based heat pipe models, and should be considered a topic for future research.

The sensitivity analysis revealed that $S_{g,crit}$ had a minor impact on steam finger growth and cluster mobilization but did proportionally increase the volume of gas in the heated zone. However, increasing the concentration of dissolved gases by 10× increased the volume of gas in the cold zone by 2.1 to 2.4×, suggesting that dissolved gases increase steam's ability to persist and flow through cold regions. This finding supports previous experimental evidence (Hegele & Mumford, 2015) that dissolved gases can play a role in ensuring that ISTT-produced gases are able to reach extraction points. This also suggests that future work on other subsurface gas applications (e.g., methane ebullition or CO_2 exsolution from leaking geological carbon storage systems) should incorporate background dissolved gas concentrations as those systems may be sensitive to their effects.

Overall, the results presented throughout this study highlight how ET-MIP provides one of the most complete frameworks for investigating highly coupled thermal/groundwater/mass transport and gas flow

scenarios. Classical continuum multiphase models are unable to capture the key features of buoyant, unstable gas flow (e.g., fingering), whereas traditional MIP models, which can describe unstable gas flow features, have no time dependence and may overestimate the rate at which gas travels. ET-MIP demonstrates that it is capable of both accurately reproducing gas flow features and, through the addition of equilibration and collapse mechanisms, is one of the only MIP models capable of limiting the rate at which steam clusters may expand and mobilize through the subsurface. With ET-MIP validated and capable of accurately reproducing local gas saturations, the capability now exists to explore simulations that examine subsurface gas behaviors such as average cluster size, lateral extension of mobilized gases, and gas front velocities.

Acknowledgments
We would like to acknowledge the support of the Natural Sciences and Engineering Research Council of Canada (NSERC). The authors would also like to acknowledge Paul Hegele for his helpful insights into the experiments used for validating the ET-MIP model. All of the model inputs required to reproduce the presented results are available from cited references. The experimental data employed to validate ET-MIP are freely available online at https://github.com/iWaterYorkU/ET-MIP-Validation-data-2019-.

References

Agaoglu, B., Scheytt, T., & Copty, N. K. (2016). Impact of NAPL architecture on interphase mass transfer: A pore network study. *Advances in Water Resources*, *95*, 138–151. https://doi.org/10.1016/j.advwatres.2015.11.012

Amili, P., & Yortsos, Y. C. (2004). Stability of heat pipes in vapor-dominated systems. *International Journal of Heat and Mass Transfer*, *47*(6-7), 1233–1246. https://doi.org/10.1016/j.ijheatmasstransfer.2003.09.015

Amos, R. T., & Mayer, U. K. (2006). Investigating the role of gas bubble formation and entrapment in contaminated aquifers: Reactive transport modelling. *Journal of Contaminant Hydrology*, *87*(1-2), 123–154. https://doi.org/10.1016/j.jconhyd.2006.04.008

Archie, G. E. (1942). The electrical resistivity log as an aid in determining some reservoir characteristics. *Transactions of the AIME*, *146*(01), 54–62. https://doi.org/10.2118/942054-g

Arps, J. J. (1953). The effect of temperature on the density and electrical resistivity of sodium chloride solutions. *Journal of Petroleum Technology*, *5*(10), 17–20. https://doi.org/10.2118/953327-G

Baker, P. E. (1973). Effect of pressure and rate on steam zone development in steamflooding. *Society of Petroleum Engineers Journal*, *13*(05), 274–284. https://doi.org/10.2118/4141-PA

Baker, R. S., & Hiester, U. (2009). Large-scale physical models of thermal remediation of DNAPL source zones in Aquitards, TERRATHERM INC FITCHBURG MA.

Baston, D. P., Falta, R. W., & Kueper, B. H. (2010). Numerical modeling of thermal conductive heating in fractured bedrock. *Groundwater*, *48*(6), 836–843. https://doi.org/10.1111/j.1745-6584.2010.00722.x

Bergman, T. L., Incropera, F. P., DeWitt, D. P., & Lavine, A. S. (2011). *Fundamentals of heat and mass transfer*. John Wiley & Sons.

Beyke, G., & Fleming, D. (2005). In situ thermal remediation of DNAPL and LNAPL using electrical resistance heating. *Remediation Journal*, *15*(3), 5–22. https://doi.org/10.1002/rem.20047

Brooks, M. C., Wise, W. R., & Annable, M. D. (1999). Fundamental changes in in situ air sparging how patterns. *Groundwater Monitoring & Remediation*, *19*(2), 105–113. https://doi.org/10.1111/j.1745-6592.1999.tb00211.x

Brooks, R. H., & Corey, A. T. (1966). Properties of porous media affecting fluid flow, *American Society of Civil Engineers Proceedings. Journal of the Irrigation and Drainage Division*, *92*(IR2), 61–88.

Butler, R. M. (1987). Rise of interfering steam chambers. *Journal of Canadian Petroleum Technology*, *26*(03). https://doi.org/10.2118/87-03-07

Cahill, A. G., Steelman, C. M., Forde, O., Kuloyo, O., Emil Ruff, S., Mayer, B., et al. (2017). Mobility and persistence of methane in groundwater in a controlled-release field experiment. *Nature Geoscience*, *10*(4), 289–294. https://doi.org/10.1038/ngeo2919

Campbell, G. S., Jungbauer, J. D. J., Bidlake, W. R., & Hungerford, R. D. (1994). Predicting the effect of temperature on soil thermal conductivity. *Soil Science*, *158*(5), 307–313. https://doi.org/10.1097/00010694-199411000-00001

Carrigan, C. R., & Nitao, J. J. (2000). Predictive and diagnostic simulation of in situ electrical heating in contaminated, low-permeability soils. *Environmental Science & Technology*, *34*(22), 4835–4841. https://doi.org/10.1021/es001506k

Chen, X., & Slater, L. (2015). Gas bubble transport and emissions for shallow peat from a northern peatland: The role of pressure changes and peat structure. *Water Resour. Res.*, *51*(1), 151–168. https://doi.org/10.1002/2014WR016268

Cirpka, O. A., & Kitanidis, P. K. (2001). Transport of volatile compounds in porous media in the presence of a trapped gas phase. *Journal of Contaminant Hydrology*, *49*(3-4), 263–285. https://doi.org/10.1016/S0169-7722(00)00196-0

Clayton, W. S. (1998). A field and laboratory investigation of air fingering during air sparging. *Groundwater Monitoring & Remediation*, *18*(3), 134–145. https://doi.org/10.1111/j.1745-6592.1998.tb00737.x

Doughty, C. (2007). Modeling geologic storage of carbon dioxide: Comparison of non hysteretic and hysteretic characteristic curves. *Energy Conversion and Management*, *48*(6), 1768–1781.

DuPont Teflon PTFE (n.d.). *Properties Handbook*, edited. DuPont Company.

Elder, C. R., & Benson, C. H. (1999). Air channel formation, size, spacing, and tortuosity during air sparging. *Groundwater Monitoring & Remediation*, *19*(3), 171–181. https://doi.org/10.1111/j.1745-6592.1999.tb00231.x

Enouy, R., Li, M., Ioannidis, M. A., & Unger, A. J. A. (2011). Gas exsolution and flow during supersaturated water injection in porous media: II. Column experiments and continuum modeling. *Advances in Water Resources*, *34*(1), 15–25. https://doi.org/10.1016/j.advwatres.2010.09.013

Ewing, R. P., & Berkowitz, B. (2001). Stochastic pore-scale growth models of DNAPL migration in porous media. *Advances in Water Resources*, *24*(3-4), 309–323. https://doi.org/10.1016/S0309-1708(00)00059-2

Falta, R. W., Pruess, K., Javandel, I., & Witherspoon, P. A. (1992). Numerical modeling of steam injection for the removal of nonaqueous phase liquids from the subsurface: 1. Numerical formulation. *Water Resources Research*, *28*(2), 433–449. https://doi.org/10.1029/91WR02526

Ganesh, P. R., Bryant, S. L., & Meckel, T. A. (2013). Characterizing small-scale migration behavior of sequestered CO_2 in a realistic geologic fabric. *Energy Procedia*, *37*, 5258–5266. https://doi.org/10.1016/j.egypro.2013.06.442

Gebhart, B., Jaluria, Y., Mahajan, R. L., & Sammakia, B. (1988). *Buoyancy-induced flows and transport* (p. 1001).

Geistlinger, H., Krauss, G., Lazik, D., & Luckner, L. (2006). Direct gas injection into saturated glass beads: Transition from incoherent to coherent gas flow pattern. *Water Resources Research*, *42*, W07403. https://doi.org/10.1029/2005WR004451

Geistlinger, H., Lazik, D., Krauss, G., & Vogel, H. J. (2009). Pore-scale and continuum modeling of gas flow pattern obtained by high-resolution optical bench-scale experiments. *Water Resources Research*, *45*, W04423. https://doi.org/10.1029/2007WR006548

Gerhard, J. I., & Kueper, B. H. (2003). Relative permeability characteristics necessary for simulating DNAPL infiltration, redistribution, and immobilization in saturated porous media. *Water Resources Research*, *39*(8), 1213. https://doi.org/10.1029/2002WR001490

Glass, R. J., Conrad, S. H., & Yarrington, L. (2001). Gravity-destabilized nonwetting phase invasion in macroheterogeneous porous media: Near-pore-scale macro modified invasion percolation simulation of experiments. *Water Resources Research*, *37*(5), 1197–1207. https://doi.org/10.1029/2000WR900294

Glass, R. J., & Yarrington, L. (2003). Mechanistic modeling of fingering, nonmonotonicity, fragmentation, and pulsation within gravity/buoyant destabilized two-phase/unsaturated flow. *Water Resources Research*, *39*(3), 1058. https://doi.org/10.1029/2002WR001542

Gomaa, E., & Somerton, W. (1974). The behavior of multifluid-saturated formations, Part II: Effect of vapor saturation—Heat pipe concept and apparent thermal conductivity, *SPE Paper*.

Gotawala, D. R., & Gates, I. D. (2008). Flow and energy dynamics at the edges of steam-assisted gravity drainage chambers, in *Canadian International Petroleum Conference*, edited, Petroleum Society of Canada, Calgary, Alberta.

Grant, G. P., & Gerhard, J. I. (2007). Simulating the dissolution of a complex dense nonaqueous phase liquid source zone: 2. Experimental validation of an interfacial area–based mass transfer model. *Water Resources Research*, *43*, W12409. https://doi.org/10.1029/2007WR006039

Hao, Y., Sun, Y., & Nitao, J. (2012). Overview of NUFT: A versatile numerical model for simulating flow and reactive transport in porous media. In *Groundwater Reactive Transport Models* (pp. 212–239). https://doi.org/10.2174/978160805306311201010212

Hegele, P. R. (2014). *Gas dynamics during bench-scale electrical resistance heating of water, TCE and dissolved CO_2*. Ontario: Queen's University, Kingston.

Hegele, P. R., & McGee, B. C. W. (2017). Managing the negative impacts of groundwater flow on electrothermal remediation. *Remediation Journal*, *27*(3), 29–38. https://doi.org/10.1002/rem.21516

Hegele, P. R., & Mumford, K. G. (2014). Gas production and transport during bench-scale electrical resistance heating of water and trichloroethene. *Journal of Contaminant Hydrology*, *165*, 24–36. https://doi.org/10.1016/j.jconhyd.2014.07.002

Hegele, P. R., & Mumford, K. G. (2015). Dissolved gas exsolution to enhance gas production and transport during bench-scale electrical resistance heating. *Advances in Water Resources*, *79*, 153–161. https://doi.org/10.1016/j.advwatres.2015.02.015

Hiebert, A. D., Vermeulen, F. E., & Chute, F. S. (1989). Application of numerical modelling to the simulation of the electric-preheat steam-drive (Epsd) process in Athabasca oil sands. *Journal of Canadian Petroleum Technology*, *28*(05).

Hiebert, A. D., Vermeulen, F. E., Chute, F. S., & Capjack, C. E. (1986). Numerical simulation results for the electrical heating of Athabasca oil-sand formations. *SPE Reservoir Engineering*, *1*(01).

Hoffman, B. T., & Kovscek, A. R. (2005). Displacement front stability of steam injection into high porosity diatomite rock. *Journal of Petroleum Science and Engineering*, *46*(4), 253–266. https://doi.org/10.1016/j.petrol.2005.01.004

Ioannidis, M. A., Chatzis, I., & Dullien, F. A. L. (1996). Macroscopic percolation model of immiscible displacement: Effects of buoyancy and spatial structure. *Water Resources Research*, *32*(11), 3297–3310. https://doi.org/10.1029/95WR02216

Ito, Y., & Ipek, G. (2005). Steam fingering phenomenon during SAGD process, in SPE International Thermal Operations and Heavy Oil Symposium, edited, Society of Petroleum Engineers, Calgary, Alberta, Canada.

Ji, W., Dahmani, A., Ahlfeld, D. P., Lin, J. D., & Hill, E. (1993). Laboratory study of air sparging: Air flow visualization. *Groundwater Monitoring & Remediation*, *13*(4), 115–126.

Johnson, J. W., Nitao, J. J., & Knauss, K. G. (2004). Reactive transport modelling of CO_2 storage in saline aquifers to elucidate fundamental processes, trapping mechanisms and sequestration partitioning. *Geological Society, London, Special Publications*, *233*(1), 107–128. https://doi.org/10.1144/GSL.SP.2004.233.01.08

Kaluarachchi, J. J. (2000). *Groundwater Contamination by Organic Pollutants*. https://doi.org/10.1061/9780784405277

Keller, M., & Stallard, R. F. (1994). Methane emission by bubbling from Gatun Lake, Panama. *Journal of Geophysical Research*, *99*(D4), 8307–8319. https://doi.org/10.1029/92JD02170

Kingston, J. L. T., Dahlen, P. R., & Johnson, P. C. (2010). State-of-the-practice review of in situ thermal technologies. *Groundwater Monitoring & Remediation*, *30*(4), 64–72. https://doi.org/10.1111/j.1745-6592.2010.01305.x

Koch, J., & Nowak, W. (2015). Predicting DNAPL mass discharge and contaminated site longevity probabilities: Conceptual model and high-resolution stochastic simulation. *Water Resources Research*, *51*, 806–831. https://doi.org/10.1002/2014WR015478

Krol, M. M., Johnson, R. L., & Sleep, B. E. (2014). An analysis of a mixed convection associated with thermal heating in contaminated porous media. *Science of The Total Environment*, *499*, 7–17. https://doi.org/10.1016/j.scitotenv.2014.08.028

Krol, M. M., Mumford, K. G., Johnson, R. L., & Sleep, B. E. (2011). Modeling discrete gas bubble formation and mobilization during subsurface heating of contaminated zones. *Advances in Water Resources*, *34*(4), 537–549. https://doi.org/10.1016/j.advwatres.2011.01.010

Krol, M. M., Sleep, B. E., & Johnson, R. L. (2011). Impact of low-temperature electrical resistance heating on subsurface flow and transport. *Water Resources Research*, *47*, W05546. https://doi.org/10.1029/2010WR009675

Kueper, B. H., & McWhorter, D. B. (1992). The use of macroscopic percolation theory to construct large-scale capillary pressure curves. *Water Resources Research*, *28*(9), 2425–2436. https://doi.org/10.1029/92WR01176

Lassen, R. N., Plampin, M., Sakaki, T., Illangasekare, T. H., Gudbjerg, J., Sonnenborg, T. O., & Jensen, K. H. (2015). Effects of geologic heterogeneity on migration of gaseous CO_2 using laboratory and modeling investigations. *International Journal of Greenhouse Gas Control*, *43*, 213–224. https://doi.org/10.1016/j.ijggc.2015.10.015

Lassen, R. N., Sonnenborg, T. O., Jensen, K. H., & Looms, M. C. (2015). Monitoring CO_2 gas-phase migration in a shallow sand aquifer using cross-borehole ground penetrating radar. *International Journal of Greenhouse Gas Control*, *37*, 287–298. https://doi.org/10.1016/j.ijggc.2015.03.030

Li, X., & Yortsos, Y. C. (1995). Theory of multiple bubble growth in porous media by solute diffusion. *Chemical Engineering Science*, *50*(8), 1247–1271. https://doi.org/10.1016/0009-2509(95)98839-7

Liu, L., Wilkinson, J., Koca, K., Buchmann, C., & Lorke, A. (2016). The role of sediment structure in gas bubble storage and release. *Journal of Geophysical Research: Biogeosciences*, *121*, 1992–2005. https://doi.org/10.1002/2016JG003456

Markle, J. M., Schincariol, R. A., Sass, J. H., & Molson, J. W. (2006). Characterizing the two-dimensional thermal conductivity distribution in a sand and gravel aquifer. *Soil Science Society of America Journal*, *70*(4), 1281–1294. https://doi.org/10.2136/sssaj2005.0293

McCray, J. E., & Falta, R. W. (1997). Numerical simulation of air sparging for remediation of NAPL contamination. *Groundwater*, *35*(1), 99–110. https://doi.org/10.1111/j.1745-6584.1997.tb00065.x

McGee, B. C. W., & Vermeulen, F. E. (2007). The mechanisms of electrical heating for the recovery of bitumen from oil sands. *Journal of Canadian Petroleum Technology*, *46*(01). https://doi.org/10.2118/07-01-03

McGuinness, M. J. (1996). Steady solution selection and existence in geothermal heat pipes—I. The convective case. *International Journal of Heat and Mass Transfer*, *39*(2), 259–274. https://doi.org/10.1016/0017-9310(95)00128-V

Miller, C. A. (1975). Stability of moving surfaces in fluid systems with heat and mass transport III. Stability of displacement fronts in porous media. *Aiche Journal*, *21*(3), 474–479. https://doi.org/10.1002/aic.690210307

Mogollón, J. M., L'Heureux, I., Dale, A. W., & Regnier, P. (2009). Methane gas-phase dynamics in marine sediments: A model study. *American Journal of Science*, *309*(3), 189–220. https://doi.org/10.2475/03.2009.01

Mumford, K. G., Dickson, S. E., & Smith, J. E. (2009). Slow gas expansion in saturated natural porous media by gas injection and partitioning with non-aqueous phase liquids. *Advances in Water Resources*, *32*(1), 29–40. https://doi.org/10.1016/j.advwatres.2008.09.006

Mumford, K. G., Hegele, P. R., & Vandenberg, G. P. (2015). Comparison of two-dimensional and three-dimensional macroscopic invasion percolation simulations with laboratory experiments of gas bubble flow in homogeneous sands. *Vadose Zone Journal*, *14*(11). https://doi.org/10.2136/vzj2015.02.0028

Mumford, K. G., Smith, J. E., & Dickson, S. E. (2010). The effect of spontaneous gas expansion and mobilization on the aqueous-phase concentrations above a dense non-aqueous phase liquid pool. *Advances in Water Resources*, *33*(4), 504–513. https://doi.org/10.1016/j.advwatres.2010.02.002

Munholland, J. L., Mumford, K. G., & Kueper, B. H. (2016). Factors affecting gas migration and contaminant redistribution in heterogeneous porous media subject to electrical resistance heating. *Journal of Contaminant Hydrology*, *184*, 14–24. https://doi.org/10.1016/j.jconhyd.2015.10.011

Nambi, I. M., & Powers, S. E. (2000). NAPL dissolution in heterogeneous systems: an experimental investigation in a simple heterogeneous system. *Journal of Contaminant Hydrology*, *44*(2), 161–184. https://doi.org/10.1016/S0169-7722(00)00095-4

O'Carroll, D. M., & Sleep, B. E. (2007). Hot water flushing for immiscible displacement of a viscous NAPL. *Journal of Contaminant Hydrology*, *91*(3-4), 247–266. https://doi.org/10.1016/j.jconhyd.2006.11.003

Oldenburg, C. M., Mukhopadhyay, S., & Cihan, A. (2016). On the use of Darcy's law and invasion-percolation approaches for modeling large-scale geologic carbon sequestration. *Greenhouse Gases: Science and Technology*, *6*(1), 19–33. https://doi.org/10.1002/ghg.1564

Oldenburg, C. M., & Unger, A. J. A. (2003). On leakage and seepage from geologic carbon sequestration sites. *Vadose Zone Journal*, *2*(3), 287–296. https://doi.org/10.2136/vzj2003.2870

Pruess, K., Oldenburg, C., & Moridis, G. (1999). TOUGH2 user's guide version 2, Ernest Orlando Lawrence Berkeley National Laboratory, Berkeley, CA (US).

Reid, R. C. (1977). *The properties of gases and liquids/Robert C. Reid, John M. Prausnitz, Thomas K. Sherwood*. New York: McGraw-Hill.

Roosevelt, S. E., & Corapcioglu, M. Y. (1998). Air bubble migration in a granular porous medium: Experimental studies. *Water Resources Research*, *34*(5), 1131–1142. https://doi.org/10.1029/98WR00371

Roy, J. W., & Smith, J. E. (2007). Multiphase flow and transport caused by spontaneous gas phase growth in the presence of dense non-aqueous phase liquid. *Journal of Contaminant Hydrology*, *89*(3-4), 251–269. https://doi.org/10.1016/j.jconhyd.2006.09.011

Samani, S. (2012). Coherent gas flow patterns in heterogeneous permeability fields from bench-scale to field-scale, Technische Universität Bergakademie Freiberg.

Satik, C., Parlar, M., & Yortsos, Y. C. (1991). A study of steady-state steam-water counterflow in porous media. *International Journal of Heat and Mass Transfer*, *34*(7), 1755–1771. https://doi.org/10.1016/0017-9310(91)90151-4

Schroth, M. H., Istok, J. D., Ahearn, S. J., & Selker, J. S. (1996). Characterization of Miller-similar silica sands for laboratory hydrologic studies. *Soil Science Society of America Journal*, *60*(5), 1331–1339. https://doi.org/10.2136/sssaj1996.03615995006000050007x

Sleep, B. E., & Sykes, J. F. (1993). Compositional simulation of groundwater contamination by organic compounds: 1. Model development and verification. *Water Resources Research*, *29*(6), 1697–1708. https://doi.org/10.1029/93WR00283

Stauffer, F., Kong, X.-Z., & Kinzelbach, W. (2009). A stochastic model for air injection into saturated porous media. *Advances in Water Resources*, *32*(8), 1180–1186. https://doi.org/10.1016/j.advwatres.2009.03.010

Stöhr, M., & Khalili, A. (2006). Dynamic regimes of buoyancy-affected two-phase flow in unconsolidated porous media. *Physical Review E*, *73*(3), 036301. https://doi.org/10.1103/PhysRevE.73.036301

Thomson, N. R., & Johnson, R. L. (2000). Air distribution during in situ air sparging: an overview of mathematical modeling. *Journal of Hazardous Materials*, *72*(2-3), 265–282. https://doi.org/10.1016/S0304-3894(99)00143-0

Tomlinson, D. W., Thomson, N. R., Johnson, R. L., & Redman, J. D. (2003). Air distribution in the Borden aquifer during in situ air sparging. *Journal of Contaminant Hydrology*, *67*(1-4), 113–132. https://doi.org/10.1016/S0169-7722(03)00070-6

Tsimpanogiannis, I. N., & Yortsos, Y. C. (2004). The critical gas saturation in a porous medium in the presence of gravity. *Journal of Colloid and Interface Science*, *270*(2), 388–395. https://doi.org/10.1016/j.jcis.2003.09.036

Udell, K. S. (1985). Heat transfer in porous media considering phase change and capillarity—The heat pipe effect. *International Journal of Heat and Mass Transfer*, *28*(2), 485–495. https://doi.org/10.1016/0017-9310(85)90082-1

Verhallen, P. T. H. M., Oomen, L. J. P., Elsen, A. J. J. M. v. d., Kruger, J., & Fortuin, J. M. H. (1984). The diffusion coefficients of helium, hydrogen, oxygen and nitrogen in water determined from the permeability of a stagnant liquid layer in the quasi-s. *Chemical Engineering Science*, *39*(11), 1535–1541. https://doi.org/10.1016/0009-2509(84)80082-2

Wagner, G., Meakin, P., Feder, J., & Jøssang, T. (1997). Buoyancy-driven invasion percolation with migration and fragmentation. *Physica A: Statistical Mechanics and its Applications*, *245*(3-4), 217–230. https://doi.org/10.1016/S0378-4371(97)00324-5

Xu, B., Yortsos, Y. C., & Salin, D. (1998). Invasion percolation with viscous forces. *Physical Review E*, *57*(1), 739–751. https://doi.org/10.1103/PhysRevE.57.739

Yortsos, Y. C., Satik, C., Bacri, J.-C., & Salin, D. (1993). Large-scale percolation theory of drainage. *Transport in Porous Media*, *10*(2), 171–195. https://doi.org/10.1007/BF00617007

Zhao, W., & Ioannidis, M. A. (2011). Gas exsolution and flow during supersaturated water injection in porous media: I. Pore network modeling. *Advances in Water Resources*, *34*(1), 2–14. https://doi.org/10.1016/j.advwatres.2010.09.010

Zuo, L., Ajo-Franklin, J. B., Voltolini, M., Geller, J. T., & Benson, S. M. (2017). Pore-scale multiphase flow modeling and imaging of CO_2 exsolution in Sandstone. *Journal of Petroleum Science and Engineering*, *155*, 63–77. https://doi.org/10.1016/j.petrol.2016.10.011